

RESEARCH ARTICLE

10.1002/2015JA022224

Special Section:

Energetic Electron Loss and its Impacts on the Atmosphere

Key Points:

- POES-based electron precipitation triggers most likely caused by EMIC waves detected on the ground
- EMIC-IPDP repeatedly triggered at a single MLT closely tied to POES-detected electron precipitation
- EMIC waves detected via POES-detected electron precipitation are primarily helium band IPDP waves

Correspondence to:

A. T. Hendry,
aaron.hendry@otago.ac.nz

Citation:

Hendry, A. T., C. J. Rodger, M. A. Clilverd, M. J. Engebretson, I. R. Mann, M. R. Lessard, T. Raita, and D. K. Milling (2016), Confirmation of EMIC wave-driven relativistic electron precipitation, *J. Geophys. Res. Space Physics*, 121, 5366–5383, doi:10.1002/2015JA022224.

Received 1 DEC 2015

Accepted 17 MAY 2016

Accepted article online 25 MAY 2016

Published online 28 JUN 2016

Confirmation of EMIC wave-driven relativistic electron precipitation

Aaron T. Hendry¹, Craig J. Rodger¹, Mark A. Clilverd², Mark J. Engebretson³, Ian R. Mann⁴, Marc R. Lessard⁵, Tero Raita⁶, and David K. Milling⁴

¹Department of Physics, University of Otago, Dunedin, New Zealand, ²British Antarctic Survey (NERC), Cambridge, UK, ³Department of Physics, Augsburg College, Minneapolis, Minnesota, USA, ⁴Department of Physics, University of Alberta, Edmonton, Alberta, Canada, ⁵Department of Physics, University of New Hampshire, Durham, New Hampshire, USA, ⁶Sodankylä Geophysical Observatory, University of Oulu, Oulu, Finland

Abstract Electromagnetic ion cyclotron (EMIC) waves are believed to be an important source of pitch angle scattering driven relativistic electron loss from the radiation belts. To date, investigations of this precipitation have been largely theoretical in nature, limited to calculations of precipitation characteristics based on wave observations and small-scale studies. Large-scale investigation of EMIC wave-driven electron precipitation has been hindered by a lack of combined wave and precipitation measurements. Analysis of electron flux data from the POES (Polar Orbiting Environmental Satellites) spacecraft has been suggested as a means of investigating EMIC wave-driven electron precipitation characteristics, using a precipitation signature particular to EMIC waves. Until now the lack of supporting wave measurements for these POES-detected precipitation events has resulted in uncertainty regarding the driver of the precipitation. In this paper we complete a statistical study comparing POES precipitation measurements with wave data from several ground-based search coil magnetometers; we further present a case study examining the global nature of this precipitation. We show that a significant proportion of the precipitation events correspond with EMIC wave detections on the ground; for precipitation events that occur directly over the magnetometers, this detection rate can be as high as 90%. Our results demonstrate that the precipitation region is often stationary in magnetic local time, narrow in L, and close to the expected plasmopause position. Predominantly, the precipitation is associated with helium band rising tone Pc1 waves on the ground. The success of this study proves the viability of POES precipitation data for investigating EMIC wave-driven electron precipitation.

1. Introduction

Electron fluxes within the radiation belts are ever-changing, reflecting the constant competition between acceleration, loss, and transport processes. Investigating the intricacies involved in each of these processes is essential to fully understand the radiation belt environment, and how particle fluxes develop during times of increased radiation belt activity. In recent years there has been an increased scientific interest in electron losses from the radiation belts and the role that these losses play in radiation belt dynamics [Friedel *et al.*, 2002; Millan and Thorne, 2007]. Some of the most important drivers of radiation belt dynamics are wave-particle interactions, which play a role in acceleration, loss, and transport processes [e.g., Thorne, 2010, and sources within]. Identifying and quantifying the effects of each of these wave-particle interactions will provide a more complete understanding of the evolution of the radiation belts during and following geomagnetic storms. Electromagnetic ion cyclotron (EMIC) waves have been identified as a potential driver of significant particle loss [Thorne and Kennel, 1971] and an understanding of the characteristics of EMIC wave-particle interactions with high-energy electrons is the focus of this study.

EMIC waves are Pc1–Pc2 (0.1–5 Hz) waves that are generated near the magnetic equator by anisotropic ring current protons [Jordanova *et al.*, 2008], produced with increased frequency during and following geomagnetic storms and substorms [Fraser *et al.*, 2010], as well as in association with magnetic compressions [Clausen *et al.*, 2011; Usanova *et al.*, 2012]. These waves are generated in one of three distinct frequency bands, i.e., below the hydrogen, helium, and oxygen ion gyrofrequencies, respectively. EMIC waves have been observed across a wide range of L shells [e.g., Meredith *et al.*, 2014; Usanova *et al.*, 2012], with some studies suggesting

preferential generation at high L shells [e.g., *Min et al.*, 2012; *Usanova et al.*, 2012], while others suggest that generation occurs more favorably near the plasmopause [e.g., *Horne and Thorne*, 1993; *Pickett et al.*, 2010]. Most studies of EMIC occurrence suggest that wave generation is focused primarily in the noon to dusk sector with limited numbers of events occurring elsewhere [e.g., *Anderson et al.*, 1992; *Halford et al.*, 2010; *Clausen et al.*, 2011; *Usanova et al.*, 2012]. Plasmaspheric plumes, located in the afternoon sector, have been reported as having EMIC occurrence rates ~ 20 times higher than nonplume regions [*Usanova et al.*, 2013]. However, recent studies using the Van Allen probes have suggested that the distribution of low-L EMIC events ($L < 5$) and He^+ band EMIC events may be more uniformly distributed in magnetic local time (MLT) space [*Saikin et al.*, 2015].

EMIC waves have long been known as a source of particle loss from the radiation belts, through cyclotron interactions with protons [e.g., *Lyons and Thorne*, 1972] and relativistic electrons [e.g., *Thorne and Kennel*, 1971], scattering the particles into the loss cone. EMIC-driven precipitation has recently come under scrutiny as a potential source of significant electron losses from the radiation belts, though there is still debate regarding the energy ranges and magnitudes of these losses.

The main limitation on EMIC-driven precipitation studies undertaken to date is the difficulty involved in obtaining simultaneous wave and electron precipitation measurements. Determining precipitation characteristics from satellite data has typically involved either theoretical calculations based on wave data [e.g., *Meredith et al.*, 2003] or on very small numbers of event-based coincident conjugate observations between satellites or ground-based stations [e.g., *Miyoshi et al.*, 2008; *Cilverd et al.*, 2015]. Ground-based observations benefit from near-constant measurements of wave data from multiple magnetometer chains worldwide; however, observations of precipitation, if they exist at all, are typically limited to model-derived values based on ionization of the upper atmosphere, which makes large-scale analysis difficult.

To date, there exist only limited observational studies investigating EMIC-driven electron precipitation. Wave data from the CRRES satellite has been used in several large-scale studies to calculate the theoretical electron precipitation energies, though these studies lack any actual precipitation measurements [e.g., *Meredith et al.*, 2003; *Ukhorskiy et al.*, 2010; *Chen et al.*, 2011; *Kersten et al.*, 2014]. A number of case studies have been published using direct observations of electron precipitation, though without corresponding wave measurements [e.g., *Bortnik et al.*, 2006; *Millan et al.*, 2002, 2007]. More recently, an increase in the number of ground-based stations capable of detecting EMIC waves as well as the launch of the Van Allen Probes has seen a number of case studies published combining both wave and electron precipitation measurements [e.g., *Miyoshi et al.*, 2008; *Rodger et al.*, 2008; *Li et al.*, 2014; *Cilverd et al.*, 2015; *Usanova et al.*, 2014]. Due to the experimental limitations of these studies, however, it is difficult to draw wholesale conclusions on EMIC wave precipitation characteristics.

A study by *Carson et al.* [2013] sought to overcome the limitations based on the lack of EMIC precipitation data by creating a database of EMIC wave events based on observations of precipitation itself. The key to this database was an EMIC-driven precipitation signature identified in Polar Operational Environmental Satellite (POES) Medium Energy Proton and Electron Detector (MEPED) data (data described in detail in section 2.1) by *Sandanger et al.* [2007, 2009]. Based on the fact that EMIC waves are potentially able to scatter both energetic protons and relativistic electrons into the loss cone, it was suggested that the presence of short-lived precipitation spikes in the POES 30–80 keV proton and >800 keV electron loss cone data should be indicative of EMIC wave activity capable of influencing the radiation belts.

Carson et al. [2013] examined 12 years of POES MEPED data (1998–2012) from the six POES spacecraft available at the time (NOAA-15 through -19 and METOP-02). These authors developed an algorithm for finding the precipitation events with the expected EMIC signature, following on from the *Sandanger et al.* [2007, 2009] reports. *Carson et al.* [2013] found 2331 wave-driven precipitation events. In the current study we have extended the observational period of the database to the end of 2014 and included data from the METOP-01 satellite, which was launched in 2012. The updated database now contains 3337 POES-detected prospective EMIC-driven precipitation events.

It is important to note that this database is not intended to be an exhaustive survey of POES-observed EMIC precipitation events, as there are several aspects that limit the effectiveness of the detection algorithm. The main limiting factor is the checks put in place to prevent false-positive detections—for this algorithm, a high specificity was favored over a high sensitivity. As a result, there are many potential events which are ignored

due to being too close to the instrument noise floor, having excessive background flux, or other such problems. It is often possible to identify by eye events that were missed by the Carson *et al.* [2013] detection algorithm, but this process is obviously far too labor intensive to consider for the POES data set in its entirety. This database also does not consider the possibility of EMIC-driven electron precipitation that occurs entirely below 800 keV. Any such events could potentially be detected using the MEPED >300 keV electron detector; however, contamination issues (described in section 2.1) significantly complicate this approach.

One of the main issues with using POES electron precipitation observations as a proxy for EMIC wave detection [Sandanger *et al.*, 2007, 2009; Carson *et al.*, 2013; Wang *et al.*, 2014] is the lack of any supporting wave measurements. The POES satellites do not carry any instruments capable of directly detecting EMIC wave activity, which makes it impossible to state conclusively that the observed precipitation is actually due to EMIC waves rather than some other driver. The ability to detect EMIC waves does exist on other satellites, for instance, the Van Allen probes; however, conjunctions between these satellites and the POES satellites are typically very rare. This makes it very difficult to investigate the validity of the EMIC precipitation database as a whole in situ. One recently reported example of such a conjunction supports the contention that the POES precipitation events reported by the Carson *et al.* [2013] algorithm are indeed produced by EMIC waves [Rodger *et al.*, 2015]. In that study a POES-reported precipitation trigger occurred within seconds of RBSP-A observing the start of an EMIC wave event, with POES located very near the base of the field line which passed through the Van Allen Probe.

Previous studies have shown that it is possible to observe EMIC waves and their resulting precipitation from the ground [e.g., Rodger *et al.*, 2008; Clilverd *et al.*, 2015]. As an initial step in this study, we will imitate this analysis for a 10 h period of EMIC activity that corresponds to a POES-detected EMIC event in the updated Carson *et al.* [2013] database. We show that for this event, there is a clear link between the POES-observed particle precipitation and EMIC waves observed on the ground. We then apply a similar analysis to the updated Carson *et al.* [2013] database as a whole, finding that a significant portion of the database events correspond with ground-based observations of EMIC waves. Finally, we provide observations from several additional magnetometers to emphasize the link between the POES-observed precipitation and the ground-based wave observations. These results all provide significant confidence that the POES-detected precipitation events are driven by EMIC waves.

2. Instrument Description

In this study we have made use of a number of ground- and satellite-based instruments to understand the link between EMIC waves and the resulting electron precipitation. These are outlined below.

2.1. POES MEPED Instrument

We use data from the Polar Operational Environmental Satellite (POES) constellation, a set of meteorological satellites in polar orbit at an altitude of ~800–850 km around the Earth. Specifically, we use the Medium Energy Proton and Electron Detector (MEPED) instrument from the second generation Space Environment Monitor (SEM-2) instrument suite. The MEPED instrument measures radiation belt electron and proton fluxes by way of four directional telescopes, two for electrons, and two for protons. These telescopes are aligned orthogonally, such that one of each of the electron and proton telescope pairs points radially outward along the Earth-to-satellite vector (the 0° detectors), while the other two telescopes point perpendicularly to these, antiparallel to the velocity vector of the satellite (the 90° detectors). These two channels approximately measure loss cone and trapped particles, respectively, though this is complicated at equatorial latitudes and near the South Atlantic Magnetic Anomaly [Rodger *et al.*, 2010a, 2010b].

Each of the directional electron telescopes measures electron flux across three different energy ranges: >30 keV, >100 keV, and >300 keV. These energy channels are referred to as the E1, E2, and E3 channels, respectively. The proton telescopes are similarly split into six different energy channels: 30–80 keV, 80–250 keV, 250–800 keV, 800–2500 keV, 2500–6900 keV, and >6900 keV. These channels are numbered P1 through P6, respectively.

Both the electron and the proton telescopes contain shielding to prevent cross contamination from occurring. In practice, however, some cross contamination still occurs. In other words, electrons above a certain energy are able to penetrate the proton detector shielding and vice versa. The exact energies at which contamination begins are not fixed, as it largely depends on the intensity of the incident flux. Roughly, the proton channels

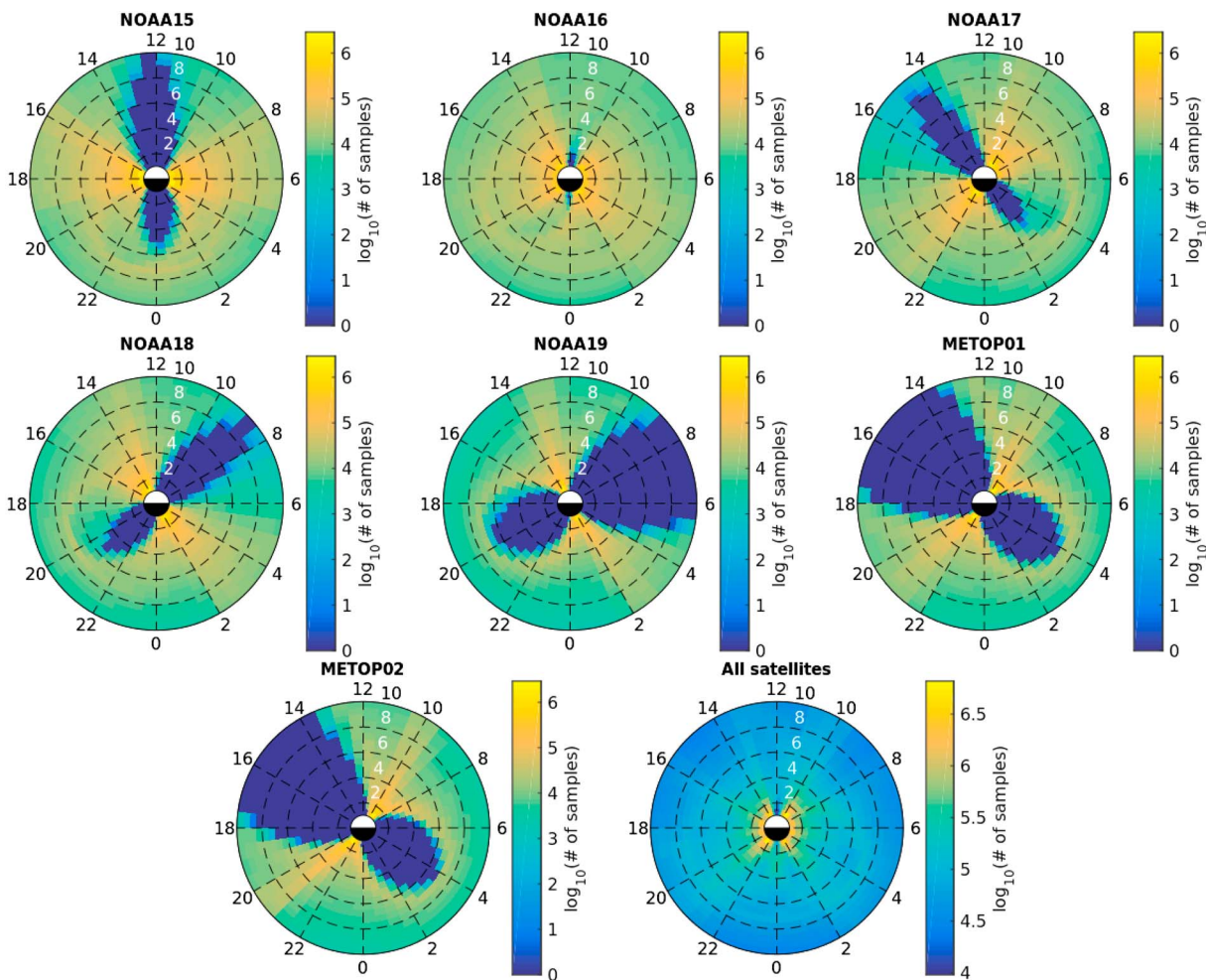


Figure 1. MLT versus L shell distributions of the POES satellites, for $1 < L < 10$. For each satellite, the location of each recorded data point is binned according to its MLT and L shell, highlighting the favored MLT regions of each satellite. (bottom right) The combined location for the observations made by of all seven POES satellites is also shown. For each plot, L shell increases radially outward from the center, while MLT increases in a counterclockwise direction with magnetic midnight at the bottom and magnetic noon at the top.

start being contaminated by electrons with energies above ~ 500 keV, while the electron channels are contaminated by protons with energies above ~ 100 keV. This contamination is particularly noticeable in the P6 proton detector, which was intended to measure high-energy protons. In the absence of high-energy protons, the P6 detector responds very strongly to relativistic electrons, allowing it to act as a fourth electron detector. A detailed description of the POES satellites and their instruments can be found in *Evans and Greer [2000]*. A full quantitative analysis of the POES MEPED contamination can be found in *Yando et al. [2011]*.

Each of the POES satellites has two preferred MLT regions, where they spend the majority of their time in orbit; this is a direct consequence of the Sun-synchronous polar orbit that each satellite is in. The MLT range sampled by each of the POES satellites is shown in Figure 1, as well as the combined MLT sampling for the combination of all of the satellites. During their operational lifetimes, many of the POES spacecraft have experienced some level of MLT drift [*Sandanger et al., 2015*], which is seen as a slight “smearing” of the data in Figure 1. This is particularly noticeable in the NOAA-16 satellite, which experienced severe drift in the later years of its operational lifetime. The MLT range of the combined POES satellite constellation (Figure 1 (bottom right)) shows significant coverage with measurements made over almost all L shells and MLT and only slightly reduced coverage for low L shells (i.e., $L < 2$) at 12 MLT. This broad coverage allows us to sample the entire MLT range in which precipitation might occur, making the POES satellites ideal for investigating particle fluxes within the radiation belts.

2.2. Ground-based Magnetometers

In addition to the POES satellite data, we also use data from several ground-based search coil magnetometers (SCM). Data are available from magnetometers operated by different institutions in various locations around the world that give broad coverage of the Pc1–Pc2 frequency range. In this study, we focus primarily on data from the Halley SCM, located at the British Antarctic Survey Halley station in Antarctica (75.6°S , 26.2°W ; $L = 4.7$). In addition to this, we also use data from a north-south chain of SCMs operated by the Sodankylä Geophysical Observatory (SGO) in Finland, the Canadian Array for Realtime Investigations of Magnetic Activity (CARISMA) chain of SCMs in Canada [Mann *et al.*, 2008], and a magnetometer in Athabasca, Canada, run by the Institute of Space-Earth Environmental Research at Nagoya University, Japan.

2.3. AARDDVARK

The Antarctic-Arctic Radiation-belt (Dynamic) Deposition-VLF Atmospheric Research Konsortium (AARDDVARK) is a global network of very low frequency (VLF) wave receivers that continuously monitor high-power, fixed-frequency VLF transmitters [Clilverd *et al.*, 2009]. The amplitude and phase of the VLF signal from these transmitters is highly sensitive to perturbations in the conductivity at the lower boundary of the ionosphere, which alter the Earth-ionosphere waveguide through which the VLF waves propagate (70–85 km). A major source of these ionospheric perturbations is electron precipitation; identifying and modeling these changes to the received signal make it possible to identify and quantify the source of the precipitation [Rodger *et al.*, 2012]. In this study we use data from two AARDDVARK stations: Halley, Antarctica, and Edmonton, Canada (53.4°N , 113.0°W ; $L = 4.2$).

2.4. Riometers

Finally, we also use data from the 30 MHz riometer located at Halley, Antarctica, and from the SGO chain of riometers in Finland. Riometers observe the relative opacity of the ionosphere by monitoring galactic radio noise passing through the ionosphere. Riometers are sensitive to changes in the ionization of the ionosphere, for instance, due to electron precipitation. Increased ionization will increase the absorption of the incident radio noise, which can be modeled to quantify the precipitation source [Little and Leinbach, 1959]. Unlike the AARDDVARK network, which is sensitive to ionospheric changes over a long path between transmitter and receiver, riometers are sensitive to ionospheric changes in a relatively small region overhead. This makes riometers useful for detecting local precipitation regions.

3. Case Study—13/14 August 2013

On 13 August 2013 at 18:01:12 UT, the Carson *et al.* [2013] algorithm detected concurrent spikes in the POES METOP-02 P1 and P6 loss cone data consistent with EMIC wave-driven precipitation. Closer examination of the data from each satellite showed 11 additional precipitation spikes consistent with EMIC-driven precipitation that did not produce triggers in the detection algorithm, primarily due to large amounts of background noise in the MEPED P1 channel. These detections occurred between 17:00 and 03:00 UT and spanned roughly a 150° longitudinal region. The L shell of each event was confined to $4 < L < 5$, i.e., close to the typical L shell of the plasmopause under nondisturbed geomagnetic conditions. The geographic location of each of these 12 detections, traced down the International Geomagnetic Reference Field (IGRF) line to an altitude of 110 km, is shown on the world map in Figure 2 as a green diamond. The IGRF conjugate locations of each event are shown as an hollow diamond. A full list of these detections and their locations is given in Table 1a.

When the geographic longitudes of the POES-detected precipitation spikes are plotted against the time of their detection, as shown in Figure 3a, there is a clear essentially constant longitudinal drift with respect to UT. The red line fitted to the points in Figure 3a represents the best fit for the drift rate of the precipitation source, with a slope of $(15.0 \pm 0.6)^{\circ}/\text{h}$. The locations of each of the POES-observed precipitation spikes in MLT are shown in Figure 3b. The red line represents the best fit for the MLT drift rate of the precipitation source, with a slope of (0.06 ± 0.07) MLT/h. The best fit is not significantly different from a slope of zero, indicating a source region that is static in MLT. These observations are consistent with a long-lived region of electron precipitation at a constant ~ 20 – 21 MLT, located close to the plasmopause, and with the expected characteristics of EMIC-driven precipitation.

Around the time that the precipitation spikes were observed in POES, clear EMIC wave signatures were observed in each of the Rovaniemi (66.8°N , 25.9°E ; $L = 5.1$), Halley, and Pinawa (50.2°N , 96.0°W ; $L = 4.0$) magnetometers. The locations of these magnetometers are shown as yellow stars in Figure 2, and a full list

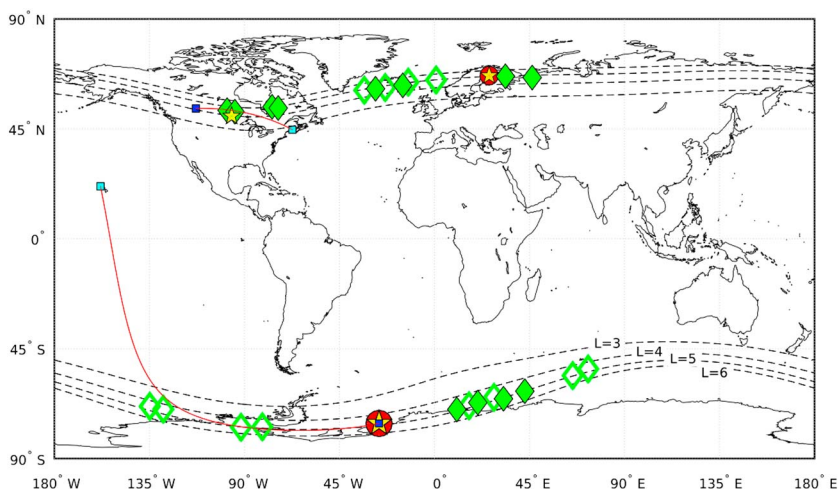


Figure 2. Map of the geographic locations of each detection of the 13 August 2013 EMIC-induced precipitation region. Red circles indicate riometer locations, yellow stars indicate search coil magnetometer locations, solid green diamonds indicate POES satellite relativistic electron precipitation locations, hollow green diamonds indicate the POES IGRF magnetic conjugate locations, light blue squares indicate VLF transmitters, and dark blue squares indicate AARDDVARK VLF receivers. The red lines indicate the great circle paths between the VLF transmitters and the AARDDVARK stations. The POES satellite locations are calculated by tracing down the IGRF field line to an altitude of 110 km. L shell contours from 3–6 are superimposed on the map.

of these detections is given in Table 1d. Several additional magnetometers from the SGO and CARISMA magnetometer chains also observed EMIC waves during the event, though with weaker power spectral density signatures.

The wave data from each of the three magnetometers named above are shown in Figure 4. Each of the three stations shows a clear rising tone EMIC wave, termed an IPDP (intervals of pulsations of diminishing periods) EMIC wave [Troitskaya, 1961], during the event period. Overlaid on the data from each magnetometer is a solid line, indicating the time in UT when the station is located at 20.5 MLT, as well as two dotted lines on either side of the solid line, indicating 1 h MLT either side. In each station, the observed wave occurs close to this MLT region, showing a clear relation between the POES-observed precipitation and the SCM observed waves. Data from the SCM located at Athabasca, Canada, situated about 20° west of Pinawa, were also checked for EMIC wave activity; however, none was observed within the specified MLT region. This is consistent with the POES-defined precipitation region, which extends no further westward than the Pinawa magnetometer, as seen in Figure 1.

Table 1a. POES Precipitation Observations^a

Time (UT)	Satellite	L Shell	MLT	Latitude (N)	Longitude (N)
2013/08/13 17:14:30	METOP-01	4.7	20.6	66.0	46.3
2013/08/13 18:01:12	METOP-02	5.0	20.5	66.5	33.6
2013/08/13 20:01:18	METOP-01	5.0	20.9	-62.4	42.8
2013/08/13 20:47:06	METOP-02	5.1	20.7	64.1	347.6
2013/08/13 21:22:44	METOP-02	4.7	20.9	62.8	345.0
2013/08/13 21:41:26	METOP-01	4.8	21.0	-67.1	20.54
2013/08/13 21:51:55	NOAA-16	4.8	20.5	61.4	332.1
2013/08/13 22:27:16	METOP-02	4.9	21.0	-69.9	10.6
2013/08/14 00:55:17	NOAA-15	5.0	19.7	51.0	283.1
2013/08/14 01:13:55	NOAA-16	4.8	20.5	53.5	286.0
2013/08/14 02:38:35	NOAA-15	4.5	19.8	52.0	265.5
2013/08/14 02:55:19	NOAA-16	4.5	20.4	52.6	261.8

^aDetailed POES observations for the 13–14 August EMIC event. The satellite locations were determined by tracing down the IGRF field line to an altitude of 110 km.

Table 1b. Magnetometer Wave Observations^a

Time Start (UT)	Time End (UT)	Location	L Shell	MLT	Latitude	Longitude
2013/08/13 17:30	2013/08/13 18:00	Rovaniemi	5.1	20.4–20.9	66.8	25.9
2013/08/13 22:15	2013/08/13 22:45	Halley	4.7	19.5–20.0	–75.6	333.8
2013/08/14 02:50	2013/08/14 03:10	Pinawa	4.1	20.2–20.5	50.2	264.0

^aDetailed magnetometer observations for the 13 - 14 August EMIC event.

These wave observations suggest that IPDP are being repeatedly triggered in a single MLT region at different UT, which are then seen by each station as they arrive at that MLT. This clearly ties the observed IPDP with the POES-observed electron precipitation regions, also seen within a single MLT region.

At the same time as their respective SCM instruments observed EMIC waves, such as that shown for Halley in Figure 5a, riometers at both the Rovaniemi and Halley stations showed sudden increases in absorption of 1.1 dB and 0.4 dB, respectively, indicative of energetic electron precipitation into the ionosphere above the instruments. Given the close temporal and spatial proximity of the wave and precipitation observations at each station, it follows that the precipitation observed in the riometers is most likely due to EMIC wave-driven electron scattering. The absorption data for the Halley riometer are shown in Figure 5b. The locations of these riometers are shown as red circles in Figure 2, and a full list of the riometer detections is given in Table 1c.

Concurrently with the riometer and SCM observations, the Halley AARDDVARK VLF receiver monitoring the Hawaii-based VLF transmitter (21.420°N, 158.2°W, 21.4 kHz, callsign NPM) observed a sudden decrease in the received amplitude of the VLF wave of about 8.2 dB. The amplitude data for the NPM VLF transmitter as seen from Halley is shown in Figure 5c (blue line), with an approximate quiet day curve shown by the red dashed line. Such a change in the VLF signal is indicative of electron precipitation somewhere along the transmitter-receiver path; the relatively small time difference between the Halley riometer and AARDDVARK observed precipitation suggests that the precipitation occurred relatively close to Halley, but along the VLF path to the west of the station.

As well as the Halley VLF receiver, the AARDDVARK VLF receiver located in Edmonton, Canada, also observed a sudden decrease of about 6.4 dB in received amplitude of the VLF signal from the Maine, USA, based transmitter (44.6°N, 67.3°W, 24.0 kHz, callsign NAA). The timing of this drop in amplitude is consistent with the POES-observed precipitation observed near the Pinawa magnetometer. The timing also agrees with the EMIC wave observed at Pinawa, which suggests that the precipitation observed along the Edmonton-NAA path likely occurred close to the Pinawa station. It is very likely that the precipitation observed by both the Halley and the Edmonton VLF receivers was due to electrons scattered by the EMIC waves detected by the nearby magnetometers. The locations of these VLF transmitters and receivers are shown as dark blue and light blue squares, respectively, in Figure 2, with red lines indicating the great circle path between them. A full description of both VLF detections is given in Table 1d.

4. Database Analysis

The *Carson et al.* [2013] database provides a useful source of potential EMIC-driven precipitation events for study; however, there remains a lingering question as to whether the majority of the events are caused by EMIC waves. Case studies such as that in the previous section show that at least some of the events in the database do correspond to actual EMIC wave events, but they say nothing of the credibility of the database as a whole. In this section we present the results of a comparison between the updated *Carson et al.* [2013] database and data from the Halley search coil magnetometer, showing that a significant proportion of the POES-detected precipitation events correspond with actual EMIC wave observations on the ground.

Table 1c. Riometer Precipitation Observations^a

Time Start (UT)	Time End (UT)	Location	L Shell	MLT	Peak Δ Absorption (dB)
2013/08/13 17:10	2013/08/13 18:10	Rovaniemi	5.1	20.1–21.1	1.1
2013/08/13 22:40	2013/08/13 22:55	Halley	4.7	20.0–20.2	0.4

^aDetailed riometer observations for the 13 - 14 August EMIC event. Station locations are the same as the relevant locations in Table 1b.

Table 1d. AARDDVARK Precipitation Observations^a

Time Start (UT)	Time End (UT)	Location	L Shell	MLT	Peak Δ Amplitude (dB)
2013/08/13 22:25	2013/08/13 22:55	Halley	4.7	19.6–20.2	–8.2
2013/08/14 02:50	2013/08/14 03:10	Edmonton	4.1	20.2–20.5	–6.4

^aDetailed AARDDVARK observations for the 13 - 14 August EMIC event. The precipitation sources occur somewhere along the path between the VLF transmitter and AARDDVARK receiver; without further modeling it is not possible to determine the exact location. For the Halley AARDDVARK receiver, the slight offset from the riometer detection in Table 1c suggests the precipitation occurred slightly east of the receiver. For the Edmonton receiver, the overlap with the Pinawa magnetometer suggests the precipitation occurred directly over Pinawa.

4.1. SCM Wave Observations

The updated Carson *et al.* [2013] event database consists of 3337 precipitation events detected between 1998 and 2014 inclusive. The Halley search coil magnetometer first started recording Pc1–Pc2 wave data in 2005, though since then it has had a few significant lapses in coverage. The main such lapse occurred in 2014, when a major electrical outage suspended all science operations at Halley for 4 months. There are also several occasions when data from the station exist but are unusable due to calibration or other issues. In total, usable Halley SCM data exist for 1915 of the 3337 POES-reported precipitation events (57%).

We want to test whether EMIC wave activity at Halley coincides with the POES-observed precipitation triggers. The case study presented in section 3 shows that there is the potential for significant longitudinal separation between a magnetometer EMIC signature and a POES precipitation trigger. Establishing the link between such widely separated observations without any intermediate wave or trigger detections is difficult, however. To avoid this issue, we restrict ourselves to only POES precipitation triggers that occur within $\pm 15^\circ$ longitude of the Halley station, the equivalent of approximately ± 1 h MLT. Due to the aggressive removal of the South Atlantic Magnetic Anomaly (SAMA) region by Carson *et al.* [2013] and the unfortunate location of the Halley

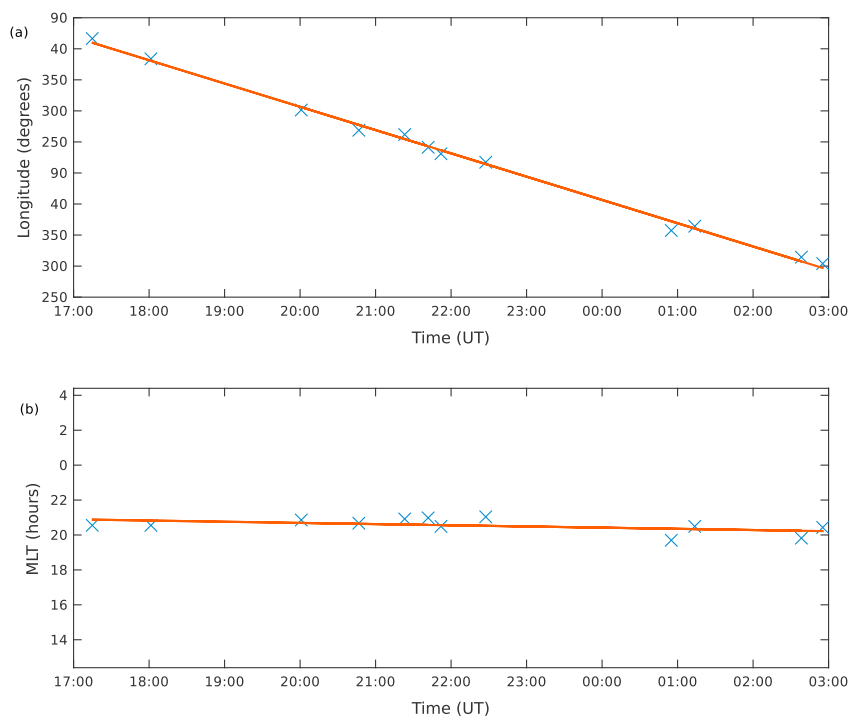


Figure 3. (a) The geographic longitude of the POES satellite-detected EMIC wave-driven electron precipitation spikes against the UT time of their detection. The longitude of the satellite is calculated by tracing the IGRF field line down from the satellite to an altitude of 110 km. These points are fitted with a linear fit, showing the longitudinal drift of the precipitation region. This line indicates a drift of approximately $15^\circ/\text{h}$. (b) The MLT location of the POES satellite-detected EMIC wave-driven electron precipitation spikes against the UT time of their detection. The y scale of this plot corresponds to the longitudinal range of the plot in Figure 3a. From this it is clear that detected precipitation spikes are approximately constant in MLT.

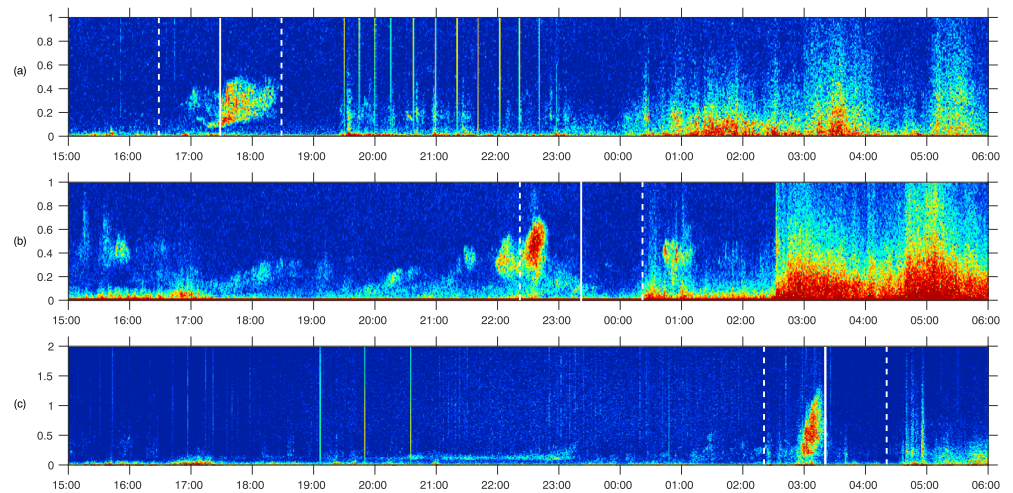


Figure 4. Search coil magnetometer data from the (a) Rovaniemi, (b) Halley, and (c) Pinawa magnetometers for the period 2013/08/13 15:00 UT to 2013/08/14 06:00 UT. The solid white lines superposed on these plots indicate the local time at each site that corresponds to 20:30 MLT, while the dashed white lines indicate 1 h MLT on either side. The wave power measured at each magnetometer is plotted in dB relative to an (different) arbitrary reference. Figures 4b and 4c show the x component of the SCM data, while Figure 4a shows the z component to avoid noisy data. In each case, the EMIC signature is clearly visible in each magnetic component.

station within this removed region, we can only consider triggers in the Northern Hemisphere, around the (IGRF) magnetic conjugate point of the Halley station (56.6° N, 304.4° E). We only include EMIC wave signatures that occur within one POES half orbit of the POES trigger (roughly ± 1 h in time).

Of the 1915 POES triggers for which there exists usable Halley SCM data, 998 of these occur in the Northern Hemisphere, of which 131 occur within $\pm 15^\circ$ longitude of the Halley magnetic conjugate point. The Carson *et al.* [2013] algorithm does not filter for multiple detections of the same precipitation event across the different POES satellites, so it is possible for a single electron precipitation event to be represented multiple times in the precipitation trigger database. Of the 131 near-Halley triggers, there were 125 unique precipitation

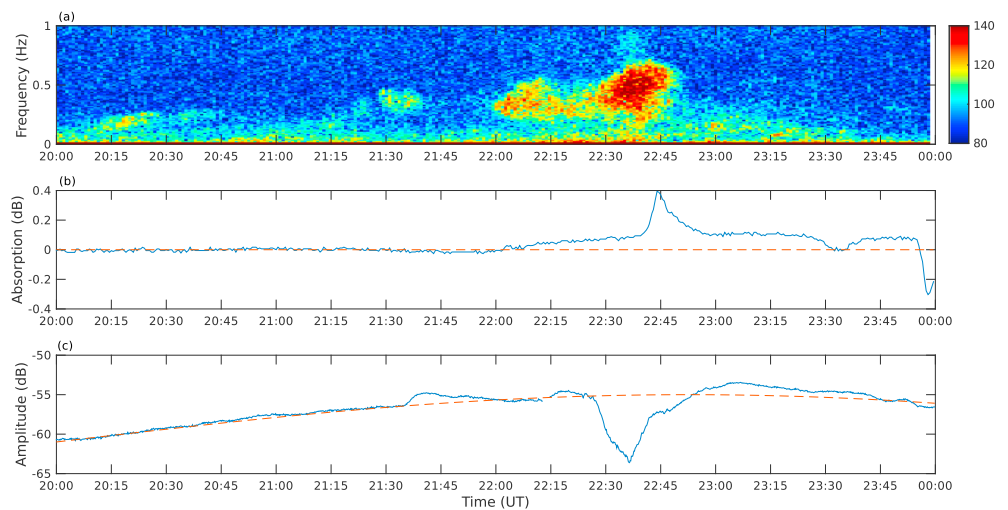


Figure 5. Observations of the 13 August 2013 EMIC wave precipitation event viewed from Halley. (a) The x component of the search coil magnetometer wave power measured at Halley, plotted in dB relative to an arbitrary reference, with a rising tone signature clearly visible from 22:30 to 22:50. (b) The Halley riometer absorption data for the event time as a solid blue line, with a dashed red line indicating the approximate quiet day curve of the riometer. (c) Amplitude data of the NPM VLF transmitter located in Hawaii, USA, as logged by the Halley AARDDVARK instrument. The blue line indicates the amplitude of the signal, while the red dotted line indicates an approximate quiet day curve for the data.

events. For each of these 125 unique events, we examined the Halley SCM data for evidence of EMIC wave activity around the time of the POES-detected precipitation.

Investigation of the Halley SCM data was carried out manually. For each event, the SCM data were examined for evidence of EMIC wave activity, namely, distinct bursts of wave power in the Pc1–Pc2 frequency range. Instances of wave power across a wide range of frequencies with no observable lower limit within the resolution of the instrument were dismissed as broadband noise and were not counted as EMIC waves. EMIC waves that exhibited a clear rising tone structure (i.e., increasing in frequency with time) were counted as IPDP-type EMIC waves. In total, 81 of the 125 unique precipitation events (64.8%) coincided with an EMIC wave observed in the Halley SCM. Around 63% of these waves were rising tone IPDP waves.

4.2. Detection Algorithm Effectiveness

In order to determine the ability of the *Carson et al.* [2013] algorithm to detect EMIC wave-driven precipitation, it is necessary to establish how often the POES-observed precipitation spikes coincide with ground-based SCM detections of EMIC waves. The above analysis based on waves observed at Halley suggests that at least 60% of the POES precipitation triggers detected by the algorithm correspond with waves on the ground. However, this still leaves the matter of the remaining 40% of events. Determining whether these “nondetections” are simply cases where the waves did not reach the Halley magnetometer or are false detections by the algorithm is important to confirming the validity of the database as a whole.

In our longitudinally restricted comparison of the POES and Halley data sets, we did not take into account the latitudinal separation of the POES satellite from Halley at the time of the POES trigger. Ducting within the Earth-ionosphere waveguide means that EMIC waves that reach the ground can be detected over a range of L shells, though the extent of this ducting is complicated. Unsurprisingly, POES triggers that have a greater latitudinal separation from Halley are less likely to have associated EMIC wave observations from the Halley station SCM. If we restrict our analysis to events that occur within $\Delta L < 1$ of the Halley magnetometer, the number of successful detections becomes 65 out of 77 events (84.4%); at $\Delta L < 0.5$ it becomes 37 out of 41 events (90.2%). This study confirms that a very high proportion of the POES triggers are associated with EMIC waves when the satellites are directly overhead of the Halley conjugate point.

The nondetection of EMIC waves from ground-based instruments, when they are known to be occurring from simultaneous space-based observations, has been reported previously. This may be due to ionospheric attenuation or absorption/reflection of the incident waves [Engebretson *et al.*, 2008]. Therefore, the absence of ground-based wave observations for the POES precipitation triggers does not necessarily indicate a false detection in the trigger data. Without further data though, for instance, in situ wave observations, it is not possible to determine whether the EMIC waves do not exist, that is, to say the POES trigger is a false detection, or if the EMIC waves are simply not reaching the ground.

4.3. Broader Database Analysis

EMIC source regions are often long-lived, as the case study presented earlier in this study shows. These long-lived source regions manifest in the data as multiple closely spaced POES precipitation triggers and SCM wave observations. In our example, the EMIC source region was constant in MLT, which resulted in a constant westward longitudinal drift of the EMIC source region footprint at a rate of $\sim 15^\circ/\text{h}$. Other previously published case studies have shown EMIC source regions that drift more rapidly in MLT, for instance, *Clilverd et al.* [2015] presented an example of an EMIC source region that crossed ~ 8.5 h of MLT in about 1.5 h (equivalent to a $\sim 85^\circ/\text{h}$ westward longitudinal drift rate).

In the previous sections, we considered POES that occurred within $\pm 15^\circ$ longitude of Halley, to maintain a strong causal link between the triggers and any observed EMIC waves in the Halley SCM data. We examined SCM data within ± 1 h of the POES trigger, which corresponds roughly to the period of a single POES half orbit. If we maintain this time restriction but allow a source region that drifts in MLT, we can consider POES triggers that occurred further away in longitude from Halley. Using the drift rates seen in the *Clilverd et al.* [2015] case study as an upper limit on source region drift rates, we are able to consider POES triggers that occurred up to $\pm 90^\circ$ in longitude away from Halley. EMIC waves seen at Halley within ± 1 h of these triggers can still conceivably be causally linked to the POES triggers, though obviously the link becomes more tenuous at greater longitudinal separation from Halley.

Using this new longitude range we have a further 408 POES triggers, in addition to the 131 near-Halley triggers investigated previously. We restrict ourselves to Northern Hemisphere triggers for consistency and to avoid

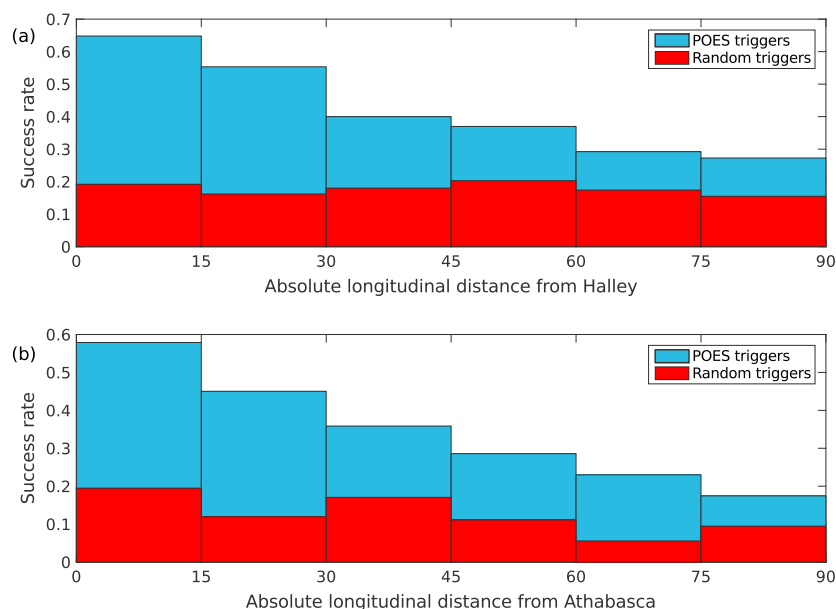


Figure 6. (a) Comparison of the EMIC wave detection success rate at Halley of the *Carson et al.* [2013] POES triggers, shown in blue, compared to triggers chosen to be independent of any precipitation spikes, shown in red. Triggers are binned by absolute longitudinal distance from Halley. (b) As above but with the Athabasca magnetometer.

any potential issues due to the SAMA region. For each of these new POES triggers we consider the Halley data, taking into account potential drift of the source region, again looking for EMIC waves that occur within an hour of the POES trigger. Due to the westward drift of the EMIC source regions, for events located eastward of Halley only SCM data recorded after the trigger time was considered, while for events westward of Halley data recorded before the trigger time was investigated. For each event, the longitudinal distance of the POES trigger from Halley was used to calculate the time lag expected between the POES trigger and any Halley EMIC observations—waves observed outside of this lag window were discounted. As before, there are instances where multiple POES satellites detected a given precipitation event. With these accounted for, there were 393 unique POES triggers observed.

In total, 167 of the 393 unique POES triggers coincided with EMIC wave observations at Halley. Unsurprisingly, the number of coincident observations between POES and Halley drops off as the longitudinal distance from Halley increases, reaching a success rate of around 25% at $\pm 90^\circ$ longitude from Halley. 43% of these EMIC waves observed at Halley were rising tone IPDP waves.

The question remains how many of these successful observations might be coincidental unrelated POES triggers and EMIC waves. To investigate the chances of a random trigger unrelated to any real precipitation spikes coinciding with an EMIC wave at Halley we generated a set of triggers independent of any POES precipitation triggers that mimicked the longitude and MLT distributions of the real triggers. We repeated the process of checking Halley for EMIC waves around these times. There is little variation in the success rate based on the distance of the random events from Halley, with an average success rate of $\sim 18\%$. A comparison of the database triggers compared to the nonprecipitation triggers is shown in Figure 6. Only 23% of these random triggers corresponded with IPDP-type EMIC waves.

There is little difference between the success rate of the randomly chosen triggers and the real triggers that occur at a distance of 75–90° longitude from Halley, suggesting that any true POES-Halley conjunctions observed at this large longitudinal separation from Halley cannot reliably be distinguished from random coincidental conjunctions. For POES triggers closer to Halley, there is a significantly increased chance above the background of observing a coincident EMIC wave at Halley.

4.4. Wave Bands

To identify the significance of the EMIC waves associated with the triggers produced by the *Carson et al.* [2013] algorithm, it is important to know which ion band the waves occur in. Previously published results have suggested that helium band EMIC waves are more likely to drive the precipitation of <2 MeV electrons than

hydrogen band EMIC [Meredith *et al.*, 2014]. The band that each of the waves is categorized into will therefore determine the relevance of the POES-detected EMIC activity to radiation belt dynamics.

The precipitation spikes in the POES data are very narrowly defined in IGRF L with each event typically occurring across an L shell range of around 0.3 L, consistent with previously published case studies, e.g., Mann *et al.* [2014]. We are therefore able to use the L shell location of the POES-observed precipitation spikes to calculate the ion gyrofrequencies at the IGRF-determined geomagnetic equator for the POES trigger locations. The IGRF magnetic field at the geomagnetic equator was calculated for each event using the International Radiation Belt Environment Modeling library (IRBEM-LIB) [Boscher *et al.*, 2015]. By comparing the calculated gyrofrequencies to the frequency ranges of the associated EMIC waves observed at Halley, we are able to determine the ion band of each wave.

Though the database is likely to include waves from each of the hydrogen, helium, and oxygen wave bands, we categorize the waves as being either hydrogen band or helium/oxygen band. The helium and oxygen wave bands are separated by the oxygen gyrofrequency; however, this separation is only with the presence of oxygen at the wave generation region. In the absence of oxygen density data, it is not possible to make the distinction between the two bands.

Of the 81 unique precipitation-causing EMIC waves observed at Halley linked to POES triggers, all but one occurred at frequencies below the POES-calculated helium gyrofrequency. Of the 167 coincident events in the broader analysis, 21 (~13%) occurred within the hydrogen band, while the rest occurred in the helium/oxygen bands.

The lack of any significant population of hydrogen band EMIC waves in those observed at Halley contrasts with previously published studies on EMIC occurrence, which show hydrogen band EMIC occurrence rates relative to other bands significantly greater than we have observed [Saikin *et al.*, 2015]. The absence of hydrogen band EMIC on the ground has been noted previously; for instance, in the case study published by Usanova *et al.* [2008], hydrogen and helium band EMIC waves were observed simultaneously in space via the Time History of Events and Macroscale Interactions during Substorms (THEMIS) satellite, but only the lower frequency helium band EMIC was observed in ground-based magnetometer data.

5. Additional Results

The conclusions from the Halley magnetometer represent only the EMIC wave behavior at a single location and do not discount the possibility of an isolated result. In this section we briefly present the results of identical studies carried out at the Athabasca ground-based magnetometer, as well as several magnetometers from the CARISMA magnetometer chain, and show that the conclusions are largely the same, regardless of the magnetometer used. As with the Halley magnetometer data, all investigations of these additional magnetometers were carried out manually.

5.1. Athabasca Magnetometer

We carried out the same investigation described in section 4 on the data from the Athabasca SCM, which provides ongoing measurements from 7 September 2005. As with the Halley magnetometer, we at first restrict our analysis to POES triggers that occur within $\pm 15^\circ$ longitude of the Athabasca SCM. The Athabasca magnetometer is far enough west in longitude that the SAMA region is not an issue, so we also include events from the Southern Hemisphere in our analysis, using the IGRF-determined magnetic conjugate point of Athabasca as the focal point. This filtering leaves us with 186 unique POES triggers, 107 of which (57.5%) occurred within ± 1 hr of EMIC waves observed at Athabasca. Further restricting these events based on their L shell separation from Athabasca increases the success rate of the detection algorithm: 87/130 (66.9%) of the events occurred for $\Delta L < 1$, while 54/67 (80.6%) of the events occurred for $\Delta L < 0.5$. Around 43% of the waves were IPDP waves, though there is a significant difference between the hemispheres (53% IPDP for triggers in the Northern Hemisphere versus 36% IPDP in the Southern Hemisphere).

We also extend the analysis to include the possibility of drifting EMIC source regions, as in section 4.3, examining POES triggers that occur within $\pm 90^\circ$ of Athabasca, in both the Northern and Southern Hemispheres. In this longitudinal range, we find 929 unique POES triggers. The 280 (30.1%) of these triggers coincided with EMIC waves observed at the Athabasca SCM, roughly 37% of which were IPDP (though again, there is a significant difference between the hemispheres, with 48% IPDP in the Northern Hemisphere versus 26% IPDP in the Southern Hemisphere). As with the Halley data, we calculate the chance that a randomly chosen POES trigger

will coincide with an EMIC wave observed in the Athabasca SCM data, with a success rate of $\sim 8\%$ across all longitudinal ranges. At distances of $75\text{--}90^\circ$ from Athabasca, the success rate of the true triggers approaches that of the random triggers. The results of this analysis are shown in Figure 6b. Only 21% of these random triggers were IPDP-type EMIC waves.

Finally, we classify each of the observed EMIC waves as being either hydrogen band or helium/oxygen band EMIC. Of the 107 wave events with POES triggers $<15^\circ$ latitude from Athabasca, only 8 (7%) occurred in the hydrogen wave band. Of the 280 events observed in the broader analysis, 64 (23%) occurred in the hydrogen wave band. Interestingly, the hydrogen band waves were observed disproportionately in the Southern Hemisphere: 30% of Southern Hemisphere events occurring in the hydrogen band, compared to only 16% of Northern Hemisphere events.

5.2. CARISMA Magnetometer Chain

The CARISMA chain of magnetometers allows us to investigate the POES triggers from multiple different latitudes along the same longitude, allowing us to determine latitudinal differences in EMIC detection. We use the magnetometers located at Fort Churchill (FCHU), Island Lake (ISLL), and Pinawa (PINA), each of which house both fluxgate and search coil magnetometers; for this study we used both types of data.

As before, we investigated Northern Hemisphere POES triggers that occurred within $\pm 15^\circ$ longitude of the magnetometers—the southern conjugate points of the CARISMA magnetometers have significant overlap with the SAMA region defined by Carson *et al.* [2013], so we do not consider the Southern Hemisphere for these magnetometers. For the FCHU, ISLL, and PINA magnetometers, respectively, we found 35/83 (42.2%), 49/89 (55.1%), and 40/85 (47.1%) unique wave/trigger conjugations, with 20%, 43%, and 63%, respectively, being IPDP EMIC waves. Extending the investigation out to include drifting source regions, we found 115/454 (25.3%), 157/497 (31.6%), and 89/339 (26.3%) wave/trigger conjugations, with 2%, 36%, and 29%, respectively, being IPDP EMIC waves. In the case of FCHU, only two of the observed EMIC waves were IPDP, suggesting a definite bias against IPDP waves at this magnetometer.

The CARISMA magnetometers show similar wave band compositions to the Halley and Athabasca magnetometers. At FCHU, only one of the events within $\pm 15^\circ$ latitude fell into the hydrogen wave band; in the broader analysis, nine of the events (8%) were hydrogen band. At ISLL, there were three (6%) hydrogen band waves within $\pm 15^\circ$ latitude and 16 (10%) in the broader analysis. At PINA, there were no hydrogen band waves within $\pm 15^\circ$ latitude and 13 (15%) in the broader analysis.

6. Spatial Distribution of EMIC Waves

As was mentioned in section 1, there have been varied reports on the distribution of EMIC waves in MLT and L space. Due to their fixed nature, using ground-based magnetometers to investigate the L shell distribution of EMIC waves is difficult. Generally, only waves that occur close to the magnetometers will be detected (where the exact definition of “close” depends on a number of factors, including the strength of the wave and the ionospheric conditions). No such difficulties exist with investigating MLT distributions, though as any given magnetometer will sample all MLT sectors over the course of a day.

Using the combined observations from Halley, Athabasca, and the CARISMA magnetometers we find that EMIC waves that coincide with a POES trigger are present across all MLT sectors. The waves show a clear preference for the afternoon and evening MLT sectors, peaking between 21 and 22 MLT. There is also a significant population in the postmidnight to morning MLT sector. Splitting the observed EMIC waves into IPDP and non-IPDP waves, we find that IPDP waves are confined almost entirely to the afternoon-evening sectors, i.e., from 15 to 22 MLT. The non-IPDP-type waves are less well confined, occurring across almost all MLT regions. The distribution of all EMIC waves observed at all magnetometers is shown in Figure 7a, with the IPDP and non-IPDP wave distributions shown in Figures 7b and 7c, respectively.

The EMIC waves observed at each magnetometer are confined to L shells relatively close to the magnetometers, reflecting the inability of the magnetometers to detect EMIC waves beyond a certain range. The L shell distribution of the waves is centered around $L = 5.1$. Splitting the waves into IPDP and non-IPDP waves again, we find that IPDP waves tend toward slightly lower L shells, with a median IPDP L shell of $L = 4.8$, compared to the non-IPDP median $L = 5.5$. The IPDP waves also tend to be more tightly clustered around the magnetometers, with 83% of IPDP waves occurring within ± 1 L shell of the magnetometers, compared to only 61% of the non-IPDP waves. The three CARISMA magnetometers also show a significant L shell dependence

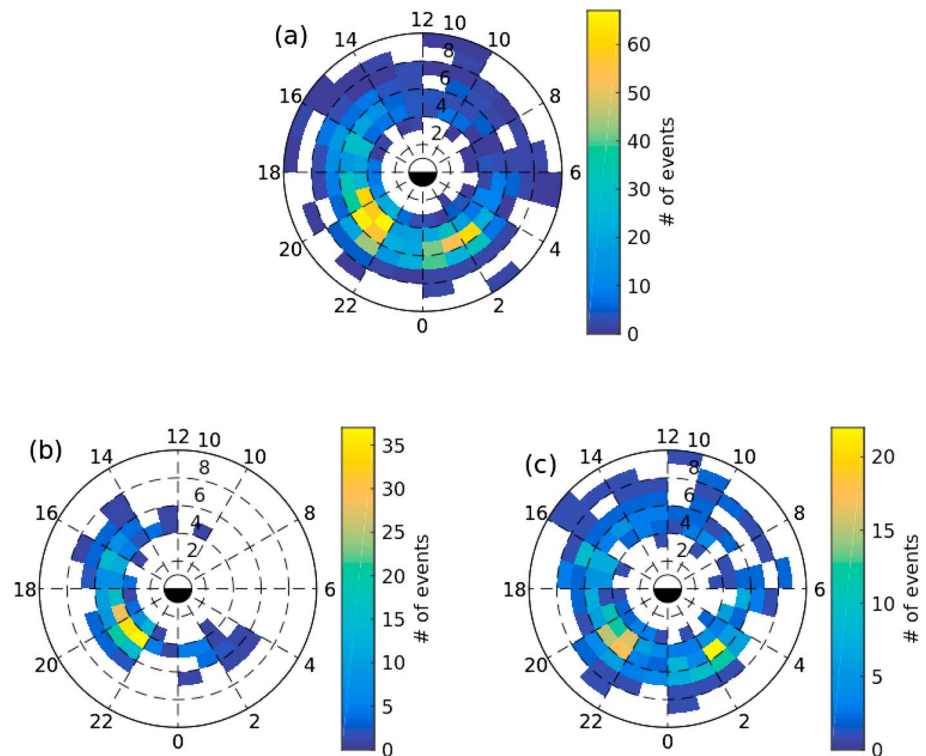


Figure 7. (a) Plot showing the distribution of all observed EMIC waves at all magnetometers, in L-MLT space. L shell is shown from 0 to 10 increasing radially outward, while MLT is shown from 0 to 24 MLT, with magnetic midnight at the 6 o'clock position. (b) As in Figure 7a but showing only the IPDP-type EMIC wave events. (c) As in Figure 7a but only showing the non-IPDP EMIC wave events.

of the IPDP waves, with the high L shell FCHU magnetometer observing very few IPDP waves, while the lower L shell ISLL and PINA magnetometers observed much greater proportions of IPDP waves.

There are distinct differences between the distributions of the hydrogen band EMIC waves and the helium/oxygen band EMIC waves. Only one of the observed hydrogen band waves occurred below $L = 5$. The hydrogen band waves occurred across all MLT sectors, with a significant peak in the postmidnight sector (1–4 MLT). By comparison, none of the helium/oxygen band EMIC waves occurred above $L = 8$, with over 50% of the waves occurring at $L < 5$. Helium band waves also occurred across all MLT sectors, though there was a significant occurrence peak in the evening sector (19–22 MLT).

7. Summary and Conclusions

From 17:00 UT on 13 August 2013 to 03:00 UT on 14 August 2013, several ground- and space-based instruments observed, both directly and indirectly, evidence of EMIC wave activity. Over this 10 h period, four of the seven POES satellites observed relativistic electron and low-energy proton precipitation spikes consistent with EMIC wave-driven scattering. The locations of these spikes suggested an EMIC source region that was static with respect to the magnetic field, centered around 20.5 MLT and $L \sim 4.8$. These observations were accompanied by ground-based observations of electron precipitation in AARD-DVARK and riometer data, consistent with the locations of the POES-observed precipitation. Additionally, several ground-based magnetometers observed rising tone EMIC waves that coincided with the timing and location of the precipitation measurements, suggesting that the IPDP EMIC waves were the cause of the precipitation.

The majority of the P6 electron precipitation spikes presented in this case study were detected manually, rather than being detected by the Carson *et al.* [2013] detection algorithm. This is a side effect of the checks put in place to prevent false-positive detections, described in the introduction to this paper. In this case study, the majority of the manually detected spikes were not flagged by the detection algorithm due to large levels of P1 proton flux, masking any potential P1 spikes from the detection algorithm. In the absence of other

evidence, the manually detected P6 electron precipitation spikes would simply be high-energy electron spikes, with no identifiable cause. However, the presence of a positive EMIC signature identified by the detection algorithm in such close proximity to the other P6 spikes, consistent with the observed EMIC wave activity, is highly suggestive of a link between the electron precipitation and the EMIC wave activity.

This event is similar to an EMIC case study recently published by *Ciliverd et al.* [2015], who showed similar conjugate observations of IPDP EMIC waves and associated precipitation using SCM, AARDDVARK, riometer, and POES instrumentation. The event investigated by *Ciliverd et al.* [2015] was short-lived, lasting only ~ 3 h UT and covering $\sim 50^\circ$ longitude; however, it was also rapidly drifting, moving through ~ 3 h MLT in this time. In comparison, the case study presented in our study was longer-lived, with observations spanning over 10 h UT and 140° longitude but static in MLT. This contrast highlights the broad range of forms that EMIC precipitation events may take.

The case study presented here, as well as the case study by *Ciliverd et al.* [2015], clearly shows the possibility for conjugate observations of EMIC activity through POES-observed precipitation and ground-based SCM wave signatures. To determine whether the link to EMIC wave activity seen in these case studies is true for the *Carson et al.* [2013] POES precipitation triggers, in general, we carried out a study of SCM data from the Halley, Antarctica station. SCM data from 2005 to 2014 was investigated, searching for signs of EMIC wave activity around the times suggested by the updated *Carson et al.* [2013] precipitation trigger database. We complemented this with similar studies using data from magnetometers located in Athabasca, Fort Churchill, Island Lake, and Pinawa, all located in Canada.

Each of the magnetometers studied showed significant numbers of EMIC waves coincident with POES electron precipitation triggers. For POES triggers that occurred within $\pm 15^\circ$ longitude of each magnetometer, including the magnetic conjugate points of the Halley and Athabasca magnetometers, we see successful detection rates of between 50 and 65%, except for the FCHU magnetometer, which sees only 42%, likely due to the high-latitude location of the magnetometer. Restricting the events further based on the L shell distance of the POES triggers from the magnetometers, we see even greater increases in successful detection rates, with the Halley magnetometer in particular detecting EMIC waves for 90% of the POES triggers that occur within $\pm 0.5L$ of the Halley Northern Hemisphere conjugate point. This suggests a very strong link between the POES-detected precipitation spikes and EMIC wave activity.

When considering the possibility of a drifting source region in MLT, we see a consistent picture across all of the magnetometers studied. For POES triggers that occur close to the magnetometers (or their magnetic conjugate points) we see high rates of successful EMIC wave observation. As the longitudinal distance from the magnetometer increases, this success rate drops off, until it approaches the “noise” success rate, i.e., the rate of successful EMIC wave detection seen for fake POES triggers with no association with any precipitation signatures.

A significant proportion of EMIC waves observed in this study were rising tone IPDP-type EMIC waves. IPDP-type waves accounted for over 50% of all EMIC waves observed when the POES triggers were $< 15^\circ$ longitude from the magnetometers. In comparison, the random triggers with no associated particle precipitation spikes only consisted of 20–25% IPDP-type waves, suggesting a preference in the *Carson et al.* [2013] algorithm toward IPDP-type waves. This indicates that IPDP-type waves may be preferentially associated with MeV electron loss as compared to Pc1 banded emissions. Further study is needed to determine if there is a significant difference between the precipitation driven by IPDP and non-IPDP EMIC waves.

The CARISMA magnetometers showed that there was a significant L shell dependence of the IPDP-type waves, with only 20% of waves observed at the high-latitude FCHU magnetometer being IPDP-type waves, compared to over 60% at the lower latitude PINA magnetometer. This suggests that IPDP-type waves are generated at lower L shells than their non-IPDP counterparts. We also saw a much lower percentage of IPDP-type waves for POES triggers $> 15^\circ$ longitude from the magnetometers. This could indicate that IPDP-type waves are less likely to drift in MLT or that they are shorter lived than non-IPDP EMIC waves. Finally, there was also a significant difference seen between the waves observed at Athabasca when comparing POES triggers in the Northern and Southern Hemispheres; Northern Hemisphere triggers were almost twice as likely to be associated with IPDP-type waves than the Southern Hemisphere triggers. Further investigation into IPDP-type waves is needed to determine the mechanisms behind these differences.

The majority of the POES precipitation-associated EMIC waves which we observed in this study occurred in the helium/oxygen bands, with only a very small portion occurring in the hydrogen band. Across all magnetometers, over 85% of observed waves occurred in the helium/oxygen bands. This possibly indicates a preference in the Carson *et al.* [2013] detection algorithm toward helium band EMIC, which might be due to differences in the characteristics of the electron precipitation scattered by the waves in each band. Alternatively, it could simply reflect the known difficulty in detecting hydrogen band EMIC waves in ground-based instruments, due to lower power or unfavorable propagation characteristics [Engebretson *et al.*, 2008; Usanova *et al.*, 2008]. Finally, it might indicate a greater difficulty for hydrogen band waves to satisfy the electron resonance condition [Denton *et al.*, 2015]. Of all of the hydrogen band waves observed in this study, only ~7% were IPDP-type waves.

We also examined the distribution of the POES trigger associated EMIC waves seen at each of the magnetometers. IPDP-type waves were restricted to the afternoon and evening MLT sectors and occurred predominantly at lower L shells. Non-IPDP EMIC waves occurred in all MLT sectors, with a peak occurring in the postmidnight sector. The helium/oxygen band waves were observed across all MLT shells with a peak in the evening sector, with over 50% of the waves occurring at $L < 5$. Hydrogen band waves were almost exclusively found at $L > 5$, again across all MLT sectors, with a peak in the postmidnight sector. Investigation of high L shell EMIC waves was limited by a lack of high-latitude magnetometer stations and by a lack of POES triggers at high L shells. This possibly indicates a preference in the Carson *et al.* [2013] detection algorithm toward lower L shell events. Alternatively, it could indicate that the higher L shell EMIC waves, which our study suggests are almost exclusively non-IPDP hydrogen band waves, are less likely to cause relativistic electron precipitation.

One aspect of the Carson *et al.* [2013] detection algorithm that still remains to be investigated is the “miss rate,” i.e., how often there is EMIC present that the algorithm fails to detect. This can happen either when there is no electron precipitation present in the energy range to which POES is sensitive or when there is excessive noise in either of the P1 or P6 loss cone channels, preventing a successful detection. We have already shown that there is a likely bias against hydrogen band waves, high L shell waves, and non-IPDP waves, possibly indicating that these types of waves do not readily precipitate electrons. A full investigation of how often the algorithm misses EMIC wave events, and the characteristics of these missed waves, is outside the scope of the current study.

The high success rate of EMIC wave detections by POES triggers located in close proximity to the magnetometers studies confirms that the Carson *et al.* [2013] detection algorithm is a valid means of detecting EMIC wave activity via POES electron precipitation data and shows that the POES precipitation trigger database is made up of a high proportion of EMIC-driven electron precipitation events. This makes it possible to use the POES precipitation data to further investigate the characteristics of the observed EMIC waves and their interactions with radiation belt electrons. The large data set of POES data (17 years of data from up to seven satellites), as well as the ease with EMIC-driven precipitation events can be automatically detected by the Carson *et al.* [2013] algorithm, makes it possible to investigate EMIC wave electron interactions on a large scale.

The POES EMIC-driven precipitation event database can also be used to complement ground-based EMIC wave detection methods. As was demonstrated in this study, data from the POES satellites can be used to determine the location of the source region of waves observed in ground-based magnetometer data. This has the potential to allow for much more detailed examination of the influence of EMIC wave ducting [cf. Mann *et al.*, 2014], as well as permitting accurate calculation of the wave band of ground-detected EMIC.

References

- Anderson, B. J., R. E. Erlandson, and L. J. Zanetti (1992), A statistical study of Pc 1–2 magnetic pulsations in the equatorial magnetosphere: 1. Equatorial occurrence distributions, *J. Geophys. Res.*, *97*(A3), 3075–3088, doi:10.1029/91JA02706.
- Bortnik, J., R. M. Thorne, T. P. O'Brien, J. C. Green, R. J. Strangeway, Y. Y. Shprits, and D. N. Baker (2006), Observation of two distinct, rapid loss mechanisms during the 20 November 2003 radiation belt dropout event, *J. Geophys. Res.*, *111*, A12216, doi:10.1029/2006JA011802.
- Boscher, D., S. Bourdarie, P. O'Brien, and T. Guild (2015), Irbem-lib - project home page. [Available at <http://irbem.sourceforge.net>.]
- Carson, B. R., C. J. Rodger, and M. A. Clilverd (2013), POES satellite observations of EMIC-wave driven relativistic electron precipitation during 1998–2010, *J. Geophys. Res. Space Physics*, *118*, 232–243, doi:10.1029/2012JA017998.
- Chen, L., R. M. Thorne, and J. Bortnik (2011), The controlling effect of ion temperature on EMIC wave excitation and scattering, *Geophys. Res. Lett.*, *38*, L16109, doi:10.1029/2011GL048653.
- Clausen, L. B. N., J. B. H. Baker, J. M. Ruohoniemi, and H. J. Singer (2011), EMIC waves observed at geosynchronous orbit during solar minimum: Statistics and excitation, *J. Geophys. Res.*, *116*, A10205, doi:10.1029/2011JA016823.
- Clilverd, M. A., et al. (2009), Remote sensing space weather events: Antarctic-Arctic Radiation-belt (Dynamic) Deposition-VLF Atmospheric Research Consortium network, *Space Weather*, *7*, S04001, doi:10.1029/2008SW000412.

Acknowledgments

The research leading to these results has received funding from the European Community's Seventh Framework Programme (FP7/2007–2013) under grant agreement 263218. The authors wish to thank the personnel who developed, maintain, and operate the NOAA/POES spacecraft; the Halley search coil magnetometer, AARDDVARK, and riometer instruments; the CARISMA search coil magnetometer chain; the Sodankylä Geophysical Observatory (SGO) search coil magnetometer and riometer chains; and the Athabasca magnetometer. Support for the Halley search coil magnetometer was provided by U.S. National Science Foundation grants PLR-1341493 to Augsburg College and PLR-1341677 to the University of New Hampshire. CARISMA is operated by the University of Alberta, funded by the Canadian Space Agency. The Athabasca induction coil magnetometer is operated by Martin Connors of the Centre for Science, Athabasca University, Athabasca, Alberta, Canada, and Kazuo Shiokawa of the Institute for Space-Earth Environmental Research, Nagoya University, Japan. The data used in this paper are available at NOAA's National Geophysical Data Center (NGDC—POES MEPED data), the British Antarctic Survey's Physical Sciences Division Data Access Framework (SCM, riometer, and AARDDVARK data), the University of Alberta CARISMA data repository (SCM data), the SGO (SCM and riometer data—available on request), and the ISEE magnetometer data site (<http://stdb2.stelab.nagoya-u.ac.jp/magne/index.html>) for all years of operation.

- Cliilverd, M. A., R. Duthie, R. Hardman, A. T. Hendry, C. J. Rodger, T. Raita, M. Engebretson, M. R. Lessard, D. Danskin, and D. K. Milling (2015), Electron precipitation from EMIC waves: A case study from 31 May 2013, *J. Geophys. Res. Space Physics*, *120*, 3618–3631, doi:10.1002/2015JA021090.
- Denton, R. E., V. K. Jordanova, and J. Bortnik (2015), Resonance of relativistic electrons with electromagnetic ion cyclotron waves, *Geophys. Res. Lett.*, *42*, 8263–8270, doi:10.1002/2015GL064379.
- Engebretson, M. J., et al. (2008), Pc1–Pc2 waves and energetic particle precipitation during and after magnetic storms: Superposed epoch analysis and case studies, *J. Geophys. Res.*, *113*, A01211, doi:10.1029/2007JA012362.
- Evans, D. S., and M. S. Greer (2000), *Polar Orbiting Environmental Satellite Space Environment Monitor-2: Instrument Description and Archive Data Documentation*, U.S. Dep. of Commer., Natl. Oceanic and Atmos. Admin., Oceanic and Atmos. Res. Lab., Space Environ. Cent., Boulder, Colo.
- Fraser, B. J., R. S. Grew, S. K. Morley, J. C. Green, H. J. Singer, T. M. Loto'aniu, and M. F. Thomsen (2010), Storm time observations of electromagnetic ion cyclotron waves at geosynchronous orbit: GOES results, *J. Geophys. Res.*, *115*, A05208, doi:10.1029/2009JA014516.
- Friedel, R. H. W., G. D. Reeves, and T. Obara (2002), Relativistic electron dynamics in the inner magnetosphere—A review, *J. Atmos. Sol. Terr. Phys.*, *64*(2), 265–282.
- Halford, A. J., B. J. Fraser, and S. K. Morley (2010), EMIC wave activity during geomagnetic storm and nonstorm periods: CRRES results, *J. Geophys. Res.*, *115*, A12248, doi:10.1029/2010JA015716.
- Horne, R. B., and R. M. Thorne (1993), On the preferred source location for the convective amplification of ion cyclotron waves, *J. Geophys. Res.*, *98*(A6), 9233–9247, doi:10.1029/92JA02972.
- Jordanova, V. K., J. Albert, and Y. Miyoshi (2008), Relativistic electron precipitation by EMIC waves from self-consistent global simulations, *J. Geophys. Res.*, *113*, A00A10, doi:10.1029/2008JA013239.
- Kersten, T., R. B. Horne, S. A. Glauert, N. P. Meredith, B. J. Fraser, and R. S. Grew (2014), Electron losses from the radiation belts caused by EMIC waves, *J. Geophys. Res. Space Physics*, *119*, 8820–8837, doi:10.1002/2014JA020366.
- Li, Z., et al. (2014), Investigation of EMIC wave scattering as the cause for the BARREL 17 January 2013 relativistic electron precipitation event: A quantitative comparison of simulation with observations, *Geophys. Res. Lett.*, *41*, 8722–8729, doi:10.1002/2014GL02273.
- Little, C., and H. Leinbach (1959), The riometer—A device for the continuous measurement of ionospheric absorption, *Proc. IRE*, *47*(2), 315–320, doi:10.1109/JRPROC.1959.287299.
- Lyons, L. R., and R. M. Thorne (1972), Parasitic pitch angle diffusion of radiation belt particles by ion cyclotron waves, *J. Geophys. Res.*, *77*(28), 5608–5616, doi:10.1029/JA077i028p05608.
- Mann, I. R., et al. (2008), The upgraded CARISMA magnetometer array in the THEMIS era, *Space Sci. Rev.*, *141*(1–4), 413–451, doi:10.1007/s11214-008-9457-6.
- Mann, I. R., M. E. Usanova, K. Murphy, M. T. Robertson, D. K. Milling, A. Kale, C. Kletzing, J. Wygant, S. Thaller, and T. Raita (2014), Spatial localization and ducting of EMIC waves: Van Allen Probes and ground-based observations, *Geophys. Res. Lett.*, *41*, 785–792, doi:10.1002/2013GL058581.
- Meredith, N. P., R. M. Thorne, R. B. Horne, D. Summers, B. J. Fraser, and R. R. Anderson (2003), Statistical analysis of relativistic electron energies for cyclotron resonance with EMIC waves observed on CRRES, *J. Geophys. Res.*, *108*(A6), 1250, doi:10.1029/2002JA009700.
- Meredith, N. P., R. B. Horne, T. Kersten, B. J. Fraser, and R. S. Grew (2014), Global morphology and spectral properties of EMIC waves derived from CRRES observations, *J. Geophys. Res. Space Physics*, *119*, 5328–5342, doi:10.1002/2014JA020064.
- Millan, R., and R. Thorne (2007), Review of radiation belt relativistic electron losses, *J. Atmos. Sol. Terr. Phys.*, *69*(3), 362–377, doi:10.1016/j.jastp.2006.06.019.
- Millan, R. M., R. P. Lin, D. M. Smith, K. R. Lorentzen, and M. P. McCarthy (2002), X-ray observations of MeV electron precipitation with a balloon-borne germanium spectrometer, *Geophys. Res. Lett.*, *29*(24), 2194, doi:10.1029/2002GL015922.
- Millan, R. M., R. P. Lin, D. M. Smith, and M. P. McCarthy (2007), Observation of relativistic electron precipitation during a rapid decrease of trapped relativistic electron flux, *Geophys. Res. Lett.*, *34*, L10101, doi:10.1029/2006GL028653.
- Min, K., J. Lee, K. Keika, and W. Li (2012), Global distribution of EMIC waves derived from THEMIS observations, *J. Geophys. Res.*, *117*, A05219, doi:10.1029/2012JA017515.
- Miyoshi, Y., K. Sakaguchi, K. Shiokawa, D. Evans, J. Albert, M. Connors, and V. Jordanova (2008), Precipitation of radiation belt electrons by EMIC waves, observed from ground and space, *Geophys. Res. Lett.*, *35*, L23101, doi:10.1029/2008GL035727.
- Pickett, J. S., et al. (2010), Cluster observations of EMIC triggered emissions in association with Pc1 waves near Earth's plasmapause, *Geophys. Res. Lett.*, *37*, L09104, doi:10.1029/2010GL042648.
- Rodger, C. J., T. Raita, M. A. Cliilverd, A. Seppälä, S. Dietrich, N. R. Thomson, and T. Ulich (2008), Observations of relativistic electron precipitation from the radiation belts driven by EMIC waves, *Geophys. Res. Lett.*, *35*, L16106, doi:10.1029/2008GL034804.
- Rodger, C. J., M. A. Cliilverd, J. C. Green, and M. M. Lam (2010a), Use of POES SEM-2 observations to examine radiation belt dynamics and energetic electron precipitation into the atmosphere, *J. Geophys. Res.*, *115*, A04202, doi:10.1029/2008JA014023.
- Rodger, C. J., B. R. Carson, S. A. Cummer, R. J. Gamble, M. A. Cliilverd, J. C. Green, J.-A. Sauvaud, M. Parrot, and J.-J. Berthelier (2010b), Contrasting the efficiency of radiation belt losses caused by ducted and nonducted whistler-mode waves from ground-based transmitters, *J. Geophys. Res.*, *115*, A12208, doi:10.1029/2010JA015880.
- Rodger, C. J., M. A. Cliilverd, A. J. Kavanagh, C. E. J. Watt, P. T. Verronen, and T. Raita (2012), Contrasting the responses of three different ground-based instruments to energetic electron precipitation, *Radio Sci.*, *47*, RS2021, doi:10.1029/2011RS004971.
- Rodger, C. J., A. T. Hendry, M. A. Cliilverd, C. A. Kletzing, J. B. Brundell, and G. D. Reeves (2015), High-resolution in-situ observations of electron precipitation-causing EMIC waves, *Geophys. Res. Lett.*, *42*, 9633–9641, doi:10.1002/2015GL066581.
- Saikin, A. A., J.-C. Zhang, R. Allen, C. W. Smith, L. M. Kistler, H. E. Spence, R. B. Torbert, C. A. Kletzing, and V. K. Jordanova (2015), The occurrence and wave properties of H⁺, He⁺, and O⁺-band EMIC waves observed by the Van Allen Probes, *J. Geophys. Res. Space Physics*, *120*, 7477–7492, doi:10.1002/2015JA021358.
- Sandanger, M., F. Søråas, K. Aarsnes, K. Oksavik, and D. S. Evans (2007), Loss of relativistic electrons: Evidence for pitch angle scattering by electromagnetic ion cyclotron waves excited by unstable ring current protons, *J. Geophys. Res.*, *112*, A12213, doi:10.1029/2006JA012138.
- Sandanger, M., F. Søråas, M. Sørbo, K. Aarsnes, K. Oksavik, and D. Evans (2009), Relativistic electron losses related to EMIC waves during CIR and CME storms, *J. Atmos. Sol. Terr. Phys.*, *71*(10–11), 1126–1144, doi:10.1016/j.jastp.2008.07.006.
- Sandanger, M. I., L.-K. G. Ødegaard, H. Nesse Tyssøy, J. Stadsnes, F. Søråas, K. Oksavik, and K. Aarsnes (2015), In-flight calibration of NOAA POES proton detectors—Derivation of the MEPED correction factors, *J. Geophys. Res. Space Physics*, *120*, 9578–9593, doi:10.1002/2015JA021388.
- Thorne, R. M. (2010), Radiation belt dynamics: The importance of wave-particle interactions, *Geophys. Res. Lett.*, *37*, L22107, doi:10.1029/2010GL044990.

- Thorne, R. M., and C. F. Kennel (1971), Relativistic electron precipitation during magnetic storm main phase, *J. Geophys. Res.*, *76*(19), 4446–4453.
- Troitskaya, V. A. (1961), Pulsation of the Earth's electromagnetic field with periods of 1 to 15 seconds and their connection with phenomena in the high atmosphere, *J. Geophys. Res.*, *66*(1), 5–18, doi:10.1029/JZ066i001p00005.
- Ukhorskiy, A. Y., Y. Y. Shprits, B. J. Anderson, K. Takahashi, and R. M. Thorne (2010), Rapid scattering of radiation belt electrons by storm-time EMIC waves, *Geophys. Res. Lett.*, *37*, L09101, doi:10.1029/2010GL042906.
- Usanova, M. E., I. R. Mann, I. J. Rae, Z. C. Kale, V. Angelopoulos, J. W. Bonnell, K.-H. Glassmeier, H. U. Auster, and H. J. Singer (2008), Multipoint observations of magnetospheric compression-related EMIC Pc1 waves by THEMIS and CARISMA, *Geophys. Res. Lett.*, *35*, L17825, doi:10.1029/2008GL034458.
- Usanova, M. E., I. R. Mann, J. Bortnik, L. Shao, and V. Angelopoulos (2012), THEMIS observations of electromagnetic ion cyclotron wave occurrence: Dependence on AE, SYMH, and solar wind dynamic pressure, *J. Geophys. Res.*, *117*, A10218, doi:10.1029/2012JA018049.
- Usanova, M. E., F. Darrouzet, I. R. Mann, and J. Bortnik (2013), Statistical analysis of EMIC waves in plasmaspheric plumes from Cluster observations, *J. Geophys. Res.*, *118*, 4946–4951, doi:10.1002/jgra.50464.
- Usanova, M. E., et al. (2014), Effect of EMIC waves on relativistic and ultrarelativistic electron populations: Ground-based and Van Allen Probes observations, *Geophys. Res. Lett.*, *41*, 1375–1381, doi:10.1002/2013GL059024.
- Wang, Z., Z. Yuan, M. Li, H. Li, D. Wang, H. Li, S. Huang, and Z. Qiao (2014), Statistical characteristics of EMIC wave-driven relativistic electron precipitation with observations of POES satellites: Revisit, *J. Geophys. Res. Space Physics*, *119*, 5509–5519, doi:10.1002/2014JA020082.
- Yando, K., R. M. Millan, J. C. Green, and D. S. Evans (2011), A Monte Carlo simulation of the NOAA POES medium energy proton and electron detector instrument, *J. Geophys. Res.*, *116*, A10231, doi:10.1029/2011JA016671.